Available online at www.sciencedirect.com

jmr&t Journal of Materials Research and Technology

journal homepage: www.elsevier.com/locate/jmrt

Original Article

Hybrid Cu-to-Cu bonding with nano-twinned Cu and non-conductive paste

Yu-Hao Kuo [a,b], Dinh-Phuc Tran [a,b], Jia-Juen Ong [a,b], K.N. Tu [c], Chih Chen [a,b,*]

[a] Department of Materials Science and Engineering, National Yang Ming Chiao Tung University, Hsinchu, 30010, Taiwan

[b] Department of Materials Science and Engineering, National Chiao Tung University, Hsinchu, 30010, Taiwan

[c] Department of Materials Science and Engineering and Department of Electrical Engineering, City University of Hong Kong, Kowloon, Hong Kong

ARTICLE INFO

Article history:
Received 15 December 2021
Accepted 2 March 2022
Available online 8 March 2022

Keywords:
Nanotwinned Cu
Hybrid bonding
Fracture modes
Grain growth

ABSTRACT

Highly (111)-oriented nanotwinned copper (nt-Cu) and non-conductive paste (NCP) were employed to fabricate hybrid Cu–Cu bonding. We tailored and correlated the fracture modes, bonding strengths, and microstructures of the joints. A non-flow underfilling process was performed, and low temperature bonding was achieved in a single heat treatment at 180 °C for 120 min without vacuum. We found that under a post-annealing treatment, recrystallization and grain growth occurred. The bonding interfaces were partially removed and the joints were further strengthened. The fracture modes of the hybrid bonding structure were characterized using pull tests and correlated with their bonding properties. Such hybrid Cu–Cu microbumps with high bonding strength and low thermal budget can be widely used for advanced ultra-fine-pitch packaging.

1. Introduction

As the world enters the artificial intelligence (AI) and 5G era, the demand for high-performance computing (HPC) chips has increased. In particular, the COVID-19 pandemic has led to huge demand for long-distance communication and work-from-home electronic devices. To enhance computing performance and further extend Moore's law, the concept of vertical integration based on three-dimensional integrated circuits (3D-ICs) was proposed [1–7]. Thus, a larger number of chips can be stacked to increase energy density [5,6,8], and the power consumed by solder joint interconnects during signal transmission can be significantly reduced [9,10]. However, the size of solder joints is required to scale down to the submicron scale for advanced 3D-IC technology. Yet, there are various reliability concerns of solder joints, such as the formations of brittle intermetallic compounds (IMC) [4,11–16], bridging during reflow, and side wall wetting (voids and/or necking) [11,12]. These have limited the scale-down efforts. Cu-to-Cu direct bonding is regarded as one of the key technologies to achieving vertical integration and to replacing solder joint interconnects.

* Corresponding author.
E-mail address: chih@mail.nctu.edu.tw (C. Chen).

https://doi.org/10.1016/j.jmrt.2022.03.009

In the semiconductor industry, low temperature bonding is of great interest, and many bonding technologies have been developed [17–29]. As chips are connected among various electronic components, a high bonding temperature will cause severe damage [30], which is of critical consideration. In the advanced packaging technology, hybrid bonding has become an important research topic in recent years. For instance, Sony Corp. has successfully employed Cu-to-Cu hybrid bonded interconnects in complementary metal-oxide-semiconductor (CMOS) image sensors [31]. In such hybrid bonding, the large mismatch of coefficient of thermal expansion (CTE) between oxide and Cu bumps (electrical interconnects) is utilized [32]. Thus, at an elevated temperature, the dishing gaps between Cu bumps are closed without an external pressure because the expansion of Cu is greater than that of oxide. Normally, a chemical mechanical planarization (CMP) step is needed to accurately control the height (Cu dishing gap) and surface roughness at bonding regions [33]. Such a complex hybrid bonding technology is costly and still in the developmental stage.

In this study, columnar grained nanotwinned copper (nt-Cu) with a high degree of (111)-orientation, electroplated by direct current [34], was used for hybrid bonding. Those nt-Cu have been proven to possess superior mechanical properties [35–38], high thermal stability [39,40], and great resistance to electromigration (EM) failures [41–44], which are applicable for low temperature bonding [45–48]. Combined with a non-conductive paste (NCP), the advantages of the two can be employed [49]. Note that a non-flow process is different from the traditional underfilling, because it requires only one heating step [50]. After dispensing the NCP, bonding can be directly carried out without a surface post-treatment. For comparison, a fine-pitch hybrid bonding using SiO_2 has been reported [51,52], which can provide good bonding but the bonding processes are unexpectedly complicated and costly. In our study, we employed nt-Cu and NCP with novel thermal strategies to fabricate Cu-to-Cu hybrid bonding. The bonding processes proposed are relatively simple and have potential for the industrial applications of ultra-fine-pitch bonding.

2. Experimental

In this study, a bump-to-film structure was fabricated. The top die (bump) with nt-Cu microbumps and highly (111)-oriented nt-Cu films were prepared. NCP was applied to prevent oxidation and to protect the bonded structure. The NCP used is a type of non-flow underfill. The Cu redistribution lines (RDLs) were first electroplated. After electroplating, a polybenzoxazole (PBO) polymer layer peeling film was immediately spin-coated onto the substrate to protect the Cu RDLs. Thus, the oxidation issue could be prevented. PBO is a thermally stable polymer with low dielectric constants and low water absorption attributing to the absent carbonyl groups in its polymer backbone. The PBO has a *Tg* of 310 °C. The composition of the residue at 550 °C does not change significantly from that of the original polymer [53]. The major decomposition occurs between 550 and 660 °C, with a total

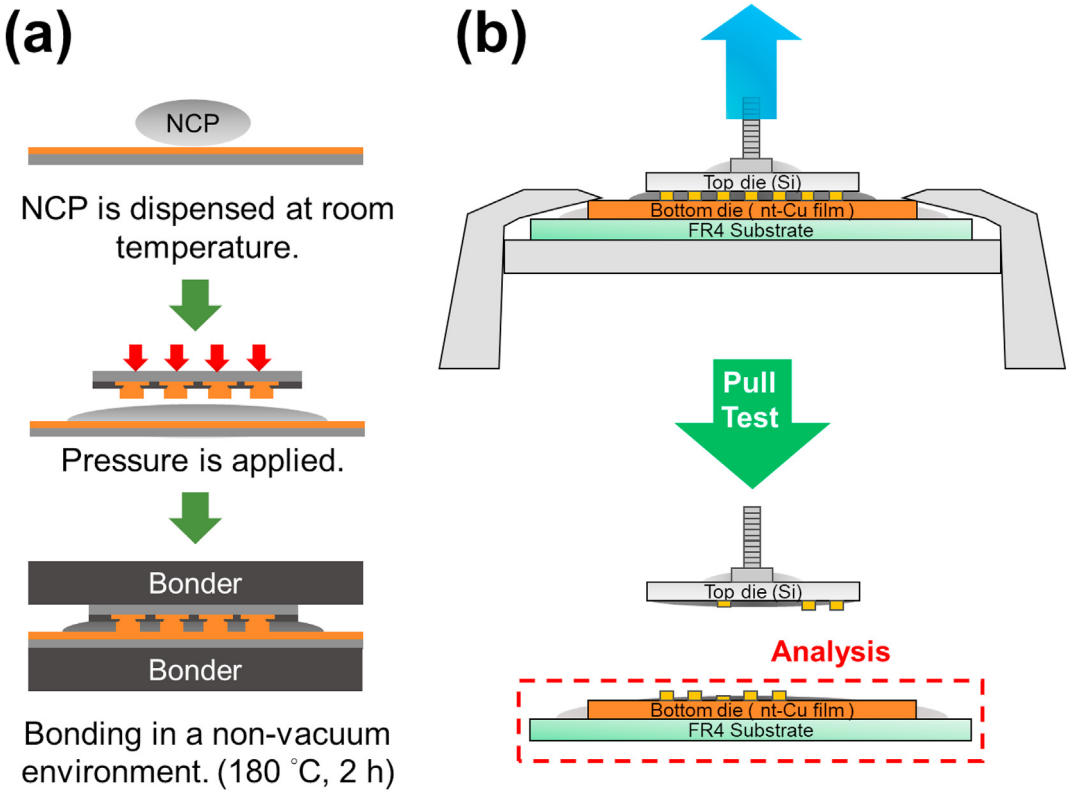

Fig. 1 – Schematic diagrams of (a) the hybrid bonding process and (b) pull test.

weight loss of 20%. At 300 °C, we believe that such a temperature did not decompose the PBO, but possibly decomposed the NCP, because the NCP (*Tg* of 100 °C) consisted of an epoxy [54]. A curing temperature of 180 °C is recommended. It remelts at 245 °C. Detailed properties of the NCP (Alpha NCX-PRL507) can be found in the technical data sheet [54]. Various passivation openings of PBO were fabricated through a lithography process, and the nt-Cu microbumps were then electroplated on and diced into several (6 x 6 mm) top dies. There were 4548 microbumps on each die. The diameter, height, and pitch of the microbumps were ~30, 15, and 80 μm, respectively.

Several nt-Cu bottom dies were electroplated by a direct current density of 80 mA/cm^2 for 3 min and electro-polished. In this study, a single crystal (100) Si substrate with predeposited Ti adhesion (100 nm) and Cu seed (200 nm) films was used. The planarized nt-Cu films (3-μm thick) were then cut into various samples with a physical dimension of 10 x 10 mm. The schematic diagram of the bonding process is shown in Fig. 1a. Before bonding, the top die and the nt-Cu film (substrate) were cleaned using acetone, isopropanol, citric acid, and deionized (DI) water. Their surfaces were then flattened through a CMP process. NCP was subsequently dispensed at room temperature on the nt-Cu film. As the top die was fully covered by the NCP, an applied force was exerted to fill the gap between the bumps.

A screw bonder was used to apply a bonding pressure (~40 MPa). We employed a screw bonder because it is easy to fix the samples on the holder or to replace a new holder. Additionally, a screw bonder is a low-cost device compared to others, thus, the experimental costs can be significantly reduced. It was then put into a tube oven. The bonding was

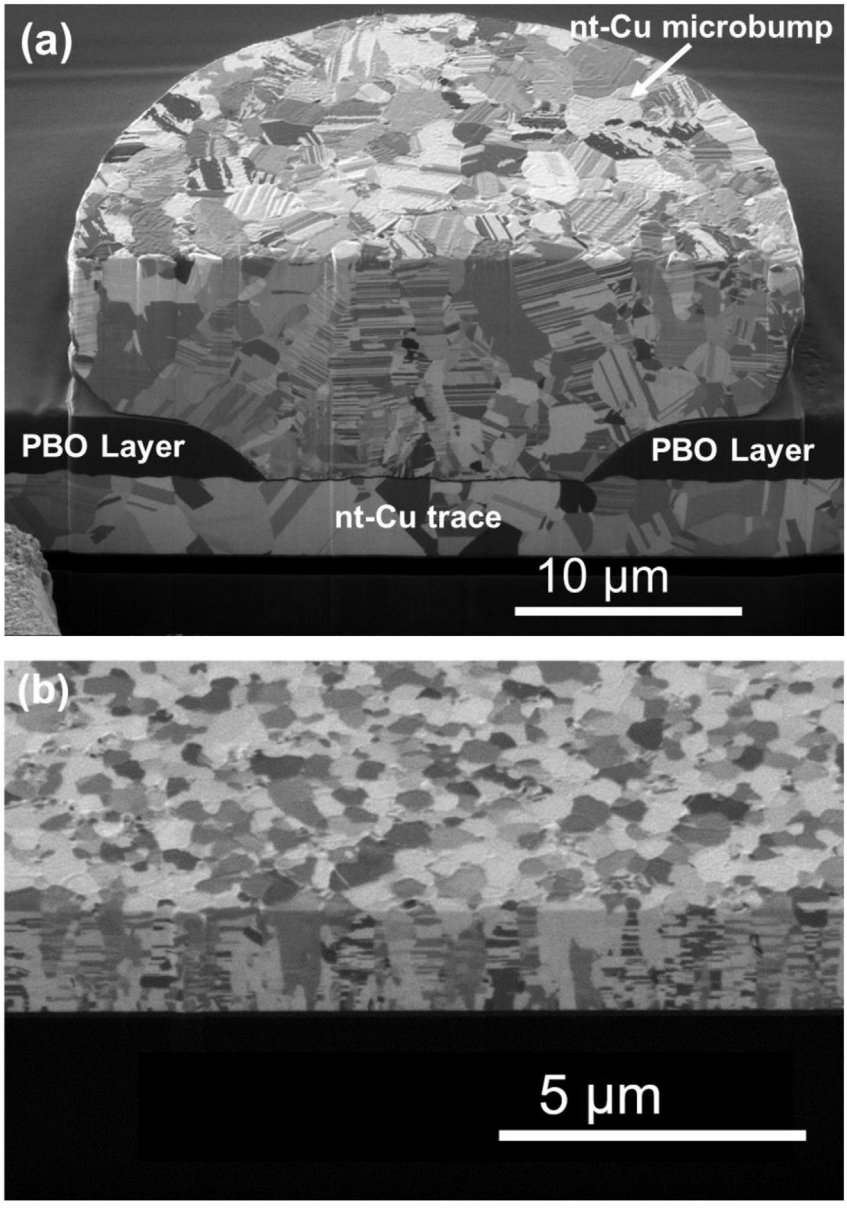

Fig. 2 – Typical cross-sectional FIB images of (a) the microbumps and (b) nt-Cu films.

annealed in air at 180 °C for 2 h. After that, a pull test was conducted to measure its bonding strength and fracture modes. Note that shearing tests are commonly used to characterize the shearing strength of joints. However, due to the small scale in shear height of the microbump samples, die shear tools may provide a non-uniform pressure causing the bending of the thin samples, leading to the combination of shearing and tension. As the bonding is increasingly deformed, its cross-section accordingly increases and the shear strength proportionally increases, leading to more severe bending. This leads to data scattering of bonding strength. Pull tests can be employed to accurately measure the bonding strength and characterize the fracture modes of very flat samples. The samples are under pure tension, thus the applied stresses on the bonding are less complicated and bonding measurements are easier to conduct. The pull tests can eliminate the thickness issues of shear tests. The schematic diagram of the pull test is shown in Fig. 1b. We focused on the bottom substrate (nt-Cu film) to characterize the fracture modes of the samples and the bumps.

The grain orientation imaging maps (OIM) of the nt-Cu film and microbumps were obtained using an electron backscattered diffraction (EBSD) system combined with a scanning electron microscope (SEM, JEOL 7800 FESEM). The surface roughness of the nt-Cu film and microbumps was examined by atomic force microscopy (AFM, Bruker Dimension Edge and Dimension Icon). A focused ion beam system (FIB, FEI Helios G3CX) was employed to observe microbump cross-sections, bonding interfaces, and NCP filling.

3. Results and discussion

Figure 2 shows the cross-sectional FIB images of the microbumps and nt-Cu films. The typical OIM and AFM images of the microbumps and nt-Cu films are shown in Fig. 3. It can be observed that the nt-Cu films were highly (111)-oriented (98.9%). The microbumps were partially (111)-oriented due to their geometry, as shown in Fig. 3a. The (111)-orientation ratio was approximately 58.5%. Some columnar grains grew

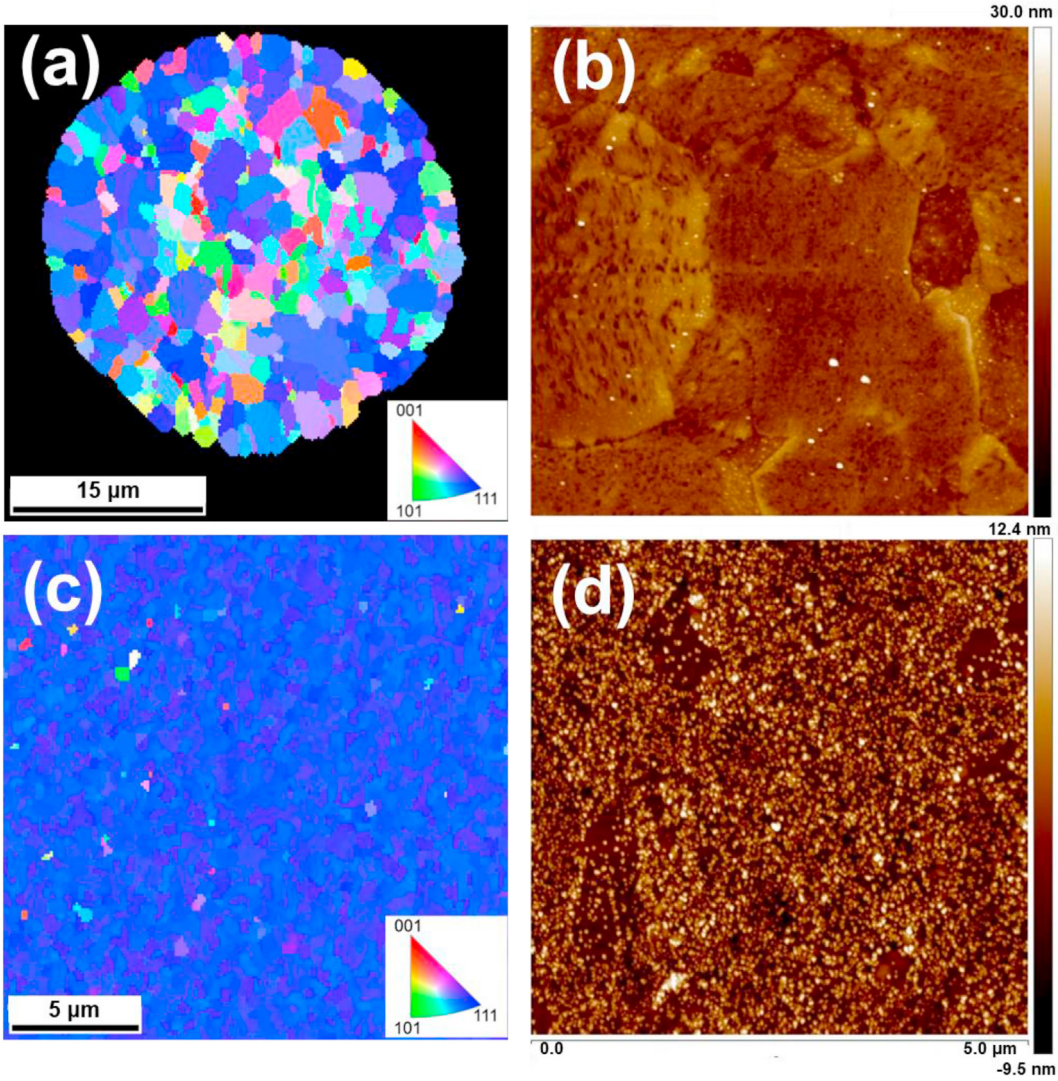

Fig. 3 – Typical OIM and AFM images of the (a,b) microbumps and (c,d) nt-Cu films, respectively.

Table 1 – Heating profiles applied for the NCP filling. Room temperature is denoted as RT.

Heating profile-A	Heating profile-B	Heating profile-C
~3 min (RT to 180 °C)	~3 min (RT to 180 °C)	~3 min (RT to 50 °C) 65 min (50–180 °C)
120 min bonding (180 °C)	180 min bonding (180 °C)	120 min bonding (180 °C)

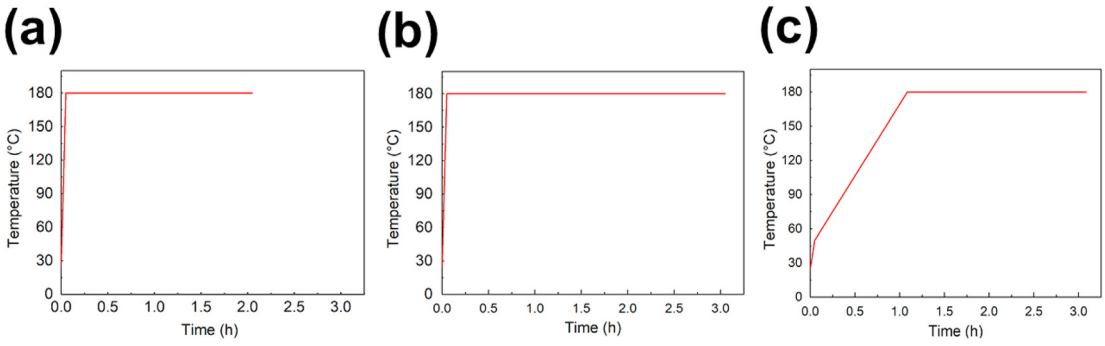

Fig. 4 – Three typical heating profiles employed to achieve the NCP filling: (a) profile-A, (b) profile-B, and (c) profile-C.

up to the surface along the PBO layer, forming a non-(111) region. Such regions were mostly scattered in the center of the microbumps. The AFM images show that the surfaces of the nt-Cu were smooth. The surface roughness (R_q) of the microbumps and nt-Cu films was ~3.5 and 2.0 nm, respectively.

In order to analyze the filling capability of the NCP, we conducted three thermal strategies, as shown in Table 1 and Fig. 4. The heating profile-A and -B show that the bonding temperatures increased rapidly to 180 °C. The temperature of profile-C was raised to 50 °C with a heating rate of 10 °C/min, and subsequently up to 180 °C with a lower rate (2 °C/min). The samples under the heating profile-C were treated at a low temperature for longer time.

Figure 5 shows the cross-sectional FIB images of the NCP filling under different heating profiles. Various bubbles were found inside the NCP filling under the heating profile-A and -B. In fact, the NCP consisted of a solvent. The bubbles were the product of pre-existing solvent and/or moisture in the NCP which undergone significant outgassing. They disappeared as

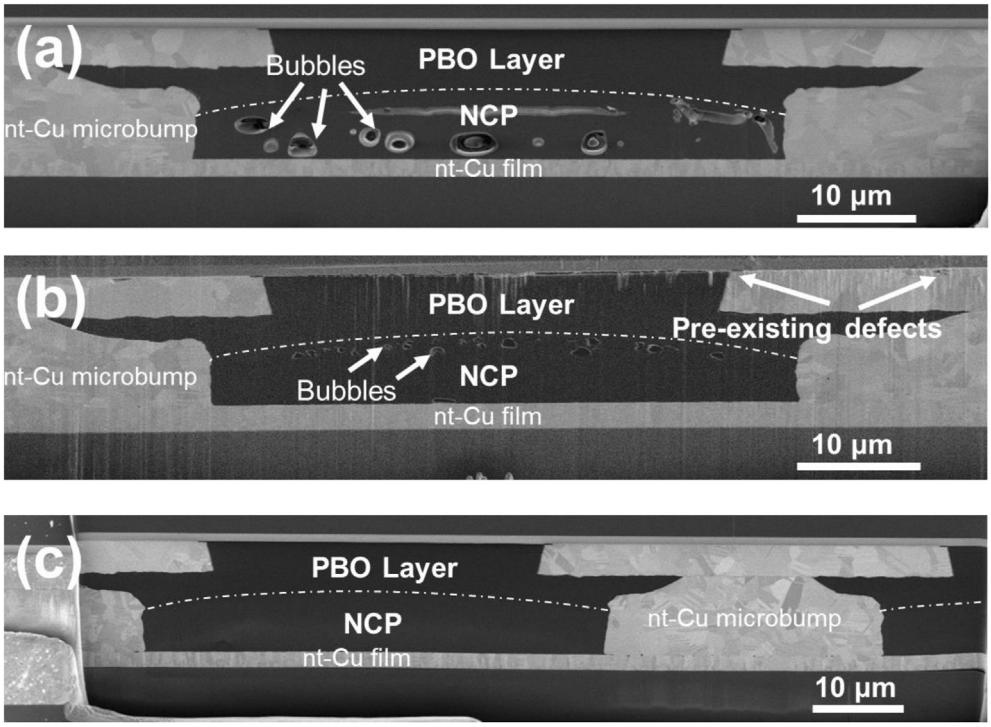

Fig. 5 – Cross-sectional FIB images of the NCP filling with different heating strategies: (a) profile-A, (b) profile-B, and (c) profile-C.

Table 2 – Detailed parameters of the two-stage bonding (Condition A and B) and the bonding (Condition C) with post-annealing.

Condition A	Condition B	Condition C
150 °C, 60 min with external pressure 180 °C, 150 min w/o external pressure	200 °C, 30 min with external pressure 180 °C, 150 min w/o external pressure	180 °C, 120 min with external pressure 300 °C, 60 min w/o external pressure

the curing temperature slowly increased. The heating rate of profile-C in the front stage was controlled. Thus, the NCP could maintain their fluidity. They were squeezed out from the bonding interface and filled the neighboring gaps. The first step (50 °C) is needed to slowly trigger the filling process. The bubbles had time to escape before curing. The heating profile

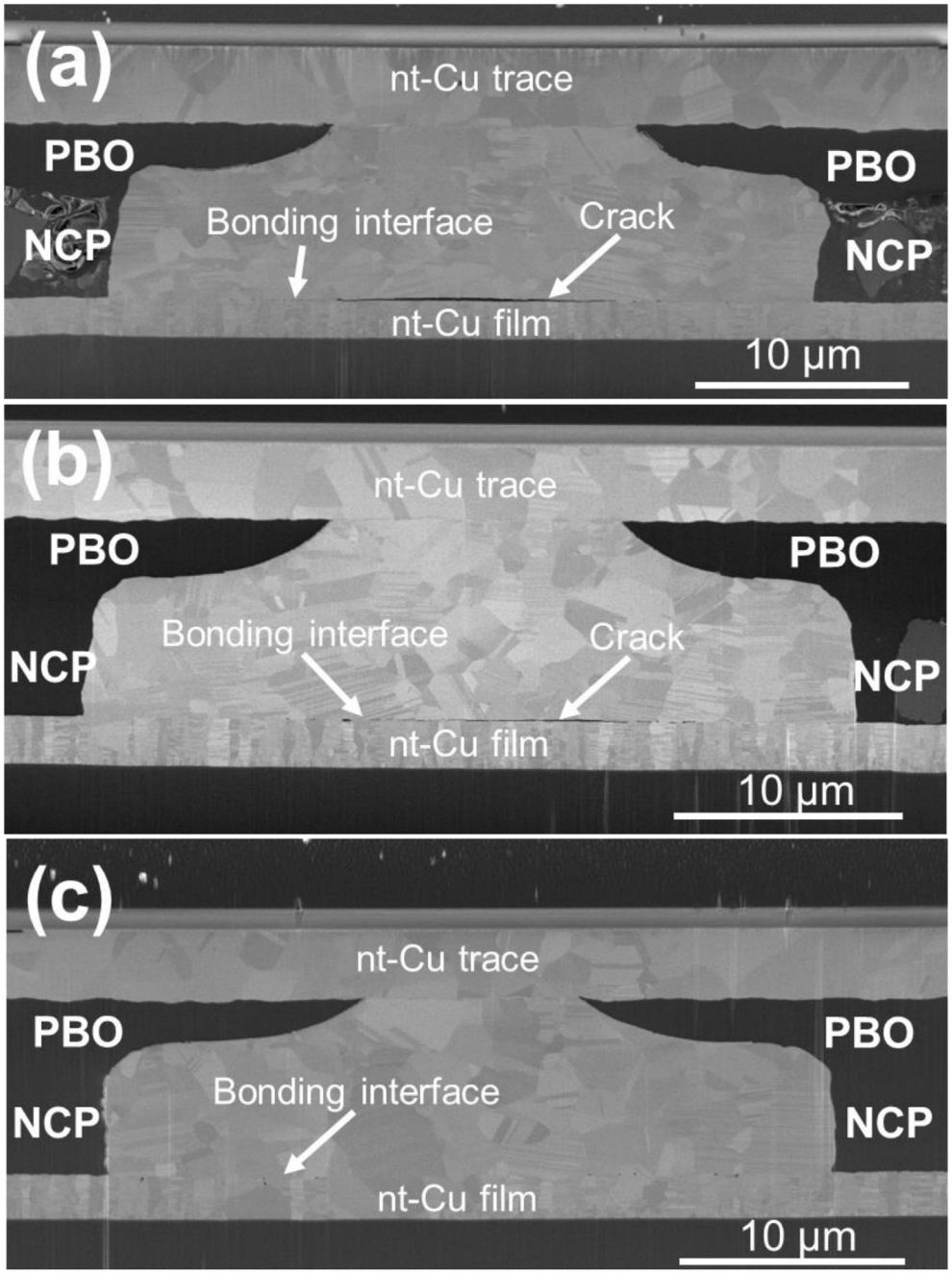

Fig. 6 – Typical cross-sectional FIB images of the nt-Cu microbumps bonded at: (a) 150 °C for 60 min and 180 °C for 150 min (two-stage bonding); (b) 200 °C for 30 min and 180 °C for 150 min (two-stage bonding); (c) 180 °C for 120 min and 300 °C for 60 min (with post-annealing).

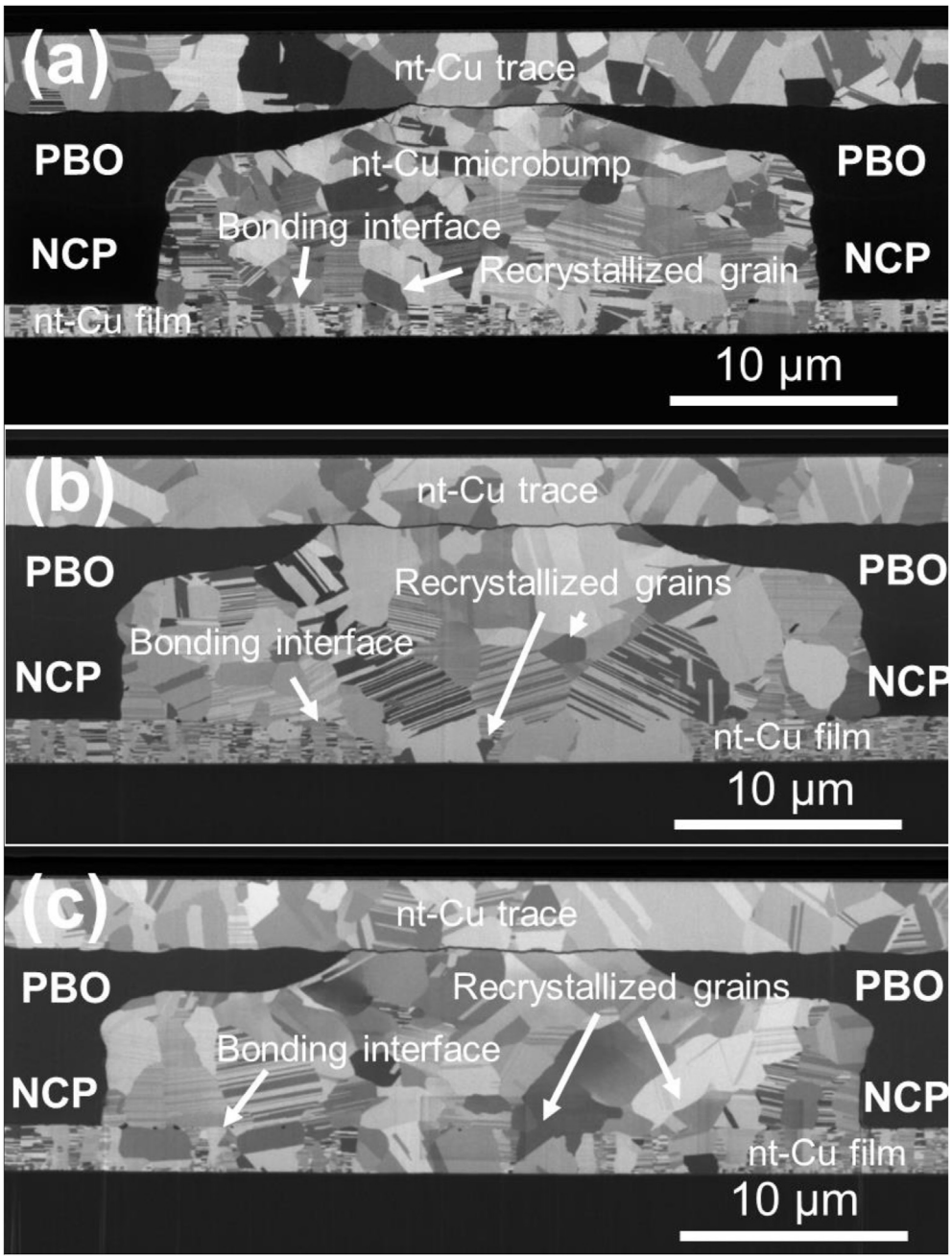

Fig. 7 – Cross-sectional FIB images of the nt-Cu microbumps bonded at (a) 180 °C for 120 min without post-annealing, (b) 180 °C for 120 min with post-annealing at 250 °C for 60 min, and (c) 180 °C for 120 min with post-annealing at 300 °C for 60 min.

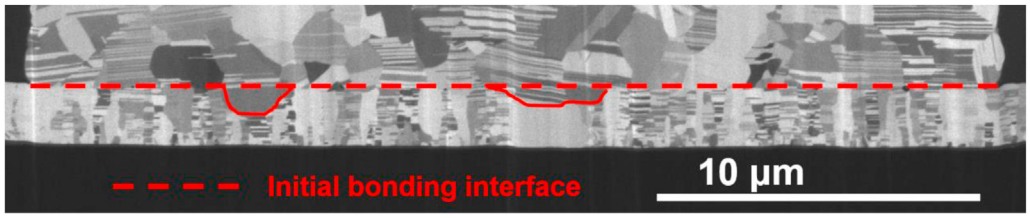

Fig. 8 – Typical cross-sectional FIB image of the microbumps bonded at 180 °C for 120 min showing a partially eliminated bonding interface.

C played an important role (65 min), and the second heating step was aimed to accelerate the filling and facilitate the curing process. As a result, a good filling was obtained by adopting the heating profile-C. Therefore, such a heating profile was chosen and conducted for further characterizations.

In this study, two-stage bonding was conducted to investigate whether the changes in bonding temperature and time could enhance the bonding of the microbumps and the curing of the NCP. The details of the bonding parameters are listed in Table 2. Note that the recommended curing parameters of the NCP are for parameter design. Ideally, the first stage of heating was employed to achieve the Cu-to-Cu bonding with an external pressure. The second stage of heating was used to cure the NCP without an applied pressure. Figure 6a and 6b shows the typical cross-sectional FIB images of the bumps after the two-stage bonding. A huge crack was observed at the center of the bonding interface. It appeared after the second heating process. It is noteworthy that the first-stage heating could not completely cure the NCP. It was further advanced by the second-stage heating. Without an external pressure, the expansions of the polymer layers (PBO and NCP) were not restricted, thus the delamination of bonding occurred. Note that the CTEs of the dielectrics (PBO and NCP) are greater than that of the Cu (two to four times). At an elevated temperature (180 or 300 °C), the middle of the Cu–Cu bumps was subjected to tensile stresses [27]. Additionally, the bonding interface can be considered as the weakest grain boundary. Therefore, cracks initiated and propagated from the pre-existing defects at the middle region of the bonding interface. Figure 6c shows the FIB image of the microbumps after post-annealing at 300 °C for 60 min. After heating twice, no obvious crack was found at the bonding interface. The NCP could be completely cured by the first-stage heating. In the second stage, even without an external pressure, the polymer layer did not further expand, preventing the delamination of the bonding interface.

Figure 7 shows the cross-sectional FIB images of the microbumps with and without post-annealing treatments. Recrystallization and grain growth can be observed in the nt-Cu films and the microbumps. Some grains grew across the bonding interface resulting in the partial elimination of the bonding interface (Fig. 7b and c). Although nt-Cu possesses high thermal stability, recrystallization and grain growth still occurred due to the pressure (40 MPa) of the screw bonder during the thermal compression bonding process. It partially eliminated the bonding interface. Note that no pressure was applied during the post-annealing, yet interfacial grain growth and recrystallization could further occur.

As shown in Fig. 7a, the bonding interface was partially eliminated, as bonded at 180 °C for 120 min. Figs. 7 b and c show the joints after post-annealing at 250 and 300 °C for 60 min, respectively. It is obvious that, after the post-annealing, various grain growth occurred in the nt-Cu films and microbumps, thus further eliminating the bonding interface. Such a phenomenon can be clearly seen in Fig. 8. The red dashed line represents the initial bonding interface. Obviously, some grains grew across the bonding interface leading to the formation of some zig zag patterns.

Additionally, the fraction of the eliminated bonding interface was estimated by measuring the lengths of the eliminated and initial interfaces, as shown in Fig. 9. We used a tool (ImageJ) to estimate the fractions in the cross-sectional FIB images. We found that the bonding quality of the microbumps was apparently enhanced by the post-annealing treatments. Figure 10 shows the bonding strength of the microbumps using pull tests. Obviously, the hybrid Cu–Cu joints were strengthened by such a heat treatment corresponding to their fraction of the eliminated bonding interface (Fig. 9). Their bonding strength was approximately doubled after the post-annealing. Such an enhancement could be attributed to the partial elimination of the bonding interface as a result of the recrystallization and grain growth across the bonding interface under the post-annealing treatment. In addition, the measured bonding strength for the joints after 250 °C for 1 h is over 30 MPa, which is comparable to those values published in literature [26,55–59].

In this study, we also characterized the bonding quality of the joints by their fracture modes. They were classified based on two viewpoints, “the samples” and “the bumps.” The

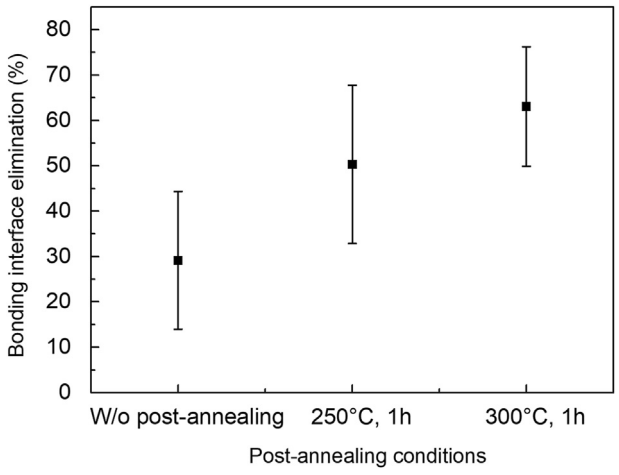

Fig. 9 – Percentage of the bonding interface elimination in the microbumps with and without post-annealing.

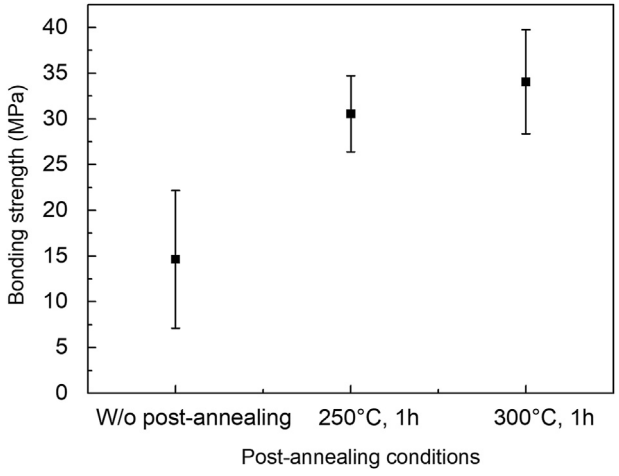

Fig. 10 – Bonding strength characteristics of the microbumps with and without post-annealing.

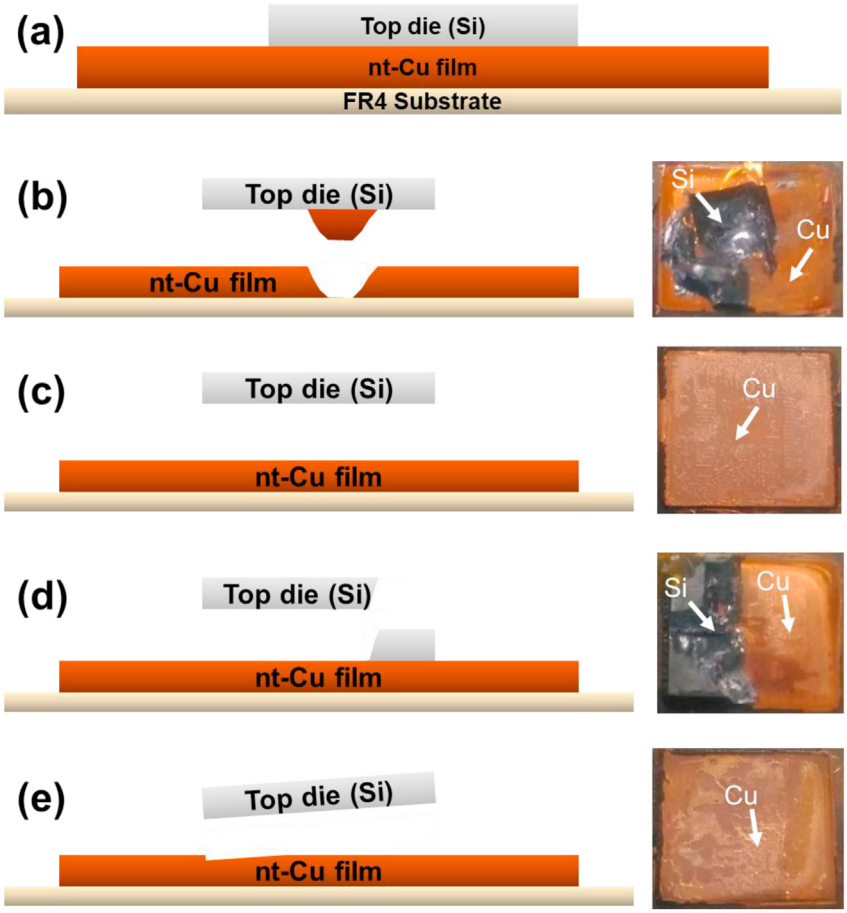

Fig. 11 – Schematic diagrams and actual images of the fracture modes of the nt-Cu bonded samples. (a) An ideal bonding between the top die and nt-Cu film. (b), (c), (d), and (e) are the fracture modes I, II, III, and IV, respectively.

fracture modes of the samples were directly qualified by observing the sample fractures after a pull test. The schematic drawings and actual images of the fracture modes are shown in Fig. 11. Herein, four fracture modes were identified. Figure 11a shows an ideal bonding between the top die and bottom film (nt-Cu film). Figure 11b shows the fracture at the bottom film, which is defined as mode I. The top die and bottom film were strongly bonded. As the top die was pulled upwards, the nt-Cu film fractured, and some partial film remained on the top die. This could be attributed to the non-uniformity of the bonding pressure. Figure 11c shows the fracture occurred as a result of a uniform bonding pressure, which is defined as mode II. The fracture surface was uniformly flat. Fracture mode III is shown in Fig. 11d. The fracture area was smaller than that of the mode II. Some regions with a poor bonding quality and/or pre-existing cracks on the top die could initially cause stress concentration in the joints and finally lead to such a fracture. Figure 11e shows the fracture due to a non-uniform bonding pressure, which is defined as mode IV. The bonding pressure in some regions (dented bonding, left) was too large while it was insufficient in the other areas (poor bonding, right). The bonding strengths of the joints (high to low) were in accordance with mode I, mode II, mode III, and mode IV.

Additionally, we characterized the fracture modes of the microbumps after pull tests using SEM. Herein, five fracture modes were identified and classified. The schematic drawings and SEM images of the fracture modes are shown in Fig. 12. An ideal bonding between the microbump and nt-Cu film is depicted in Fig. 12a. In Fig. 12b, it shows that the microbump and Cu RDL maintained on top of the nt-Cu film because the bonding strength of the microbump and nt-Cu film was extremely high. We define it as an RDL fracture. Figure 12c shows that the microbump was partially removed, which is defined as a volcano-shaped fracture. Figure 12d shows a bump-RDL fracture on the passivation opening, and we define it as a passivation opening fracture. The bonding strength between the microbump and nt-Cu film was greater than that between the bump and nt-Cu RDL. Stress concentration likely appeared in the small area of the passivation opening. Figure 12e and f shows similar fractures at the bonding interface between the microbump and nt-Cu film. They can be defined as polymer layer peeling and bonding interface fractures, respectively. These were due to the low bonding quality of the microbump and nt-Cu film. The bonding strengths of the microbumps (classified from high to low) were in correspondence with RDL, volcano-shaped, passivation opening, polymer layer peeling, and bonding interface fractures.

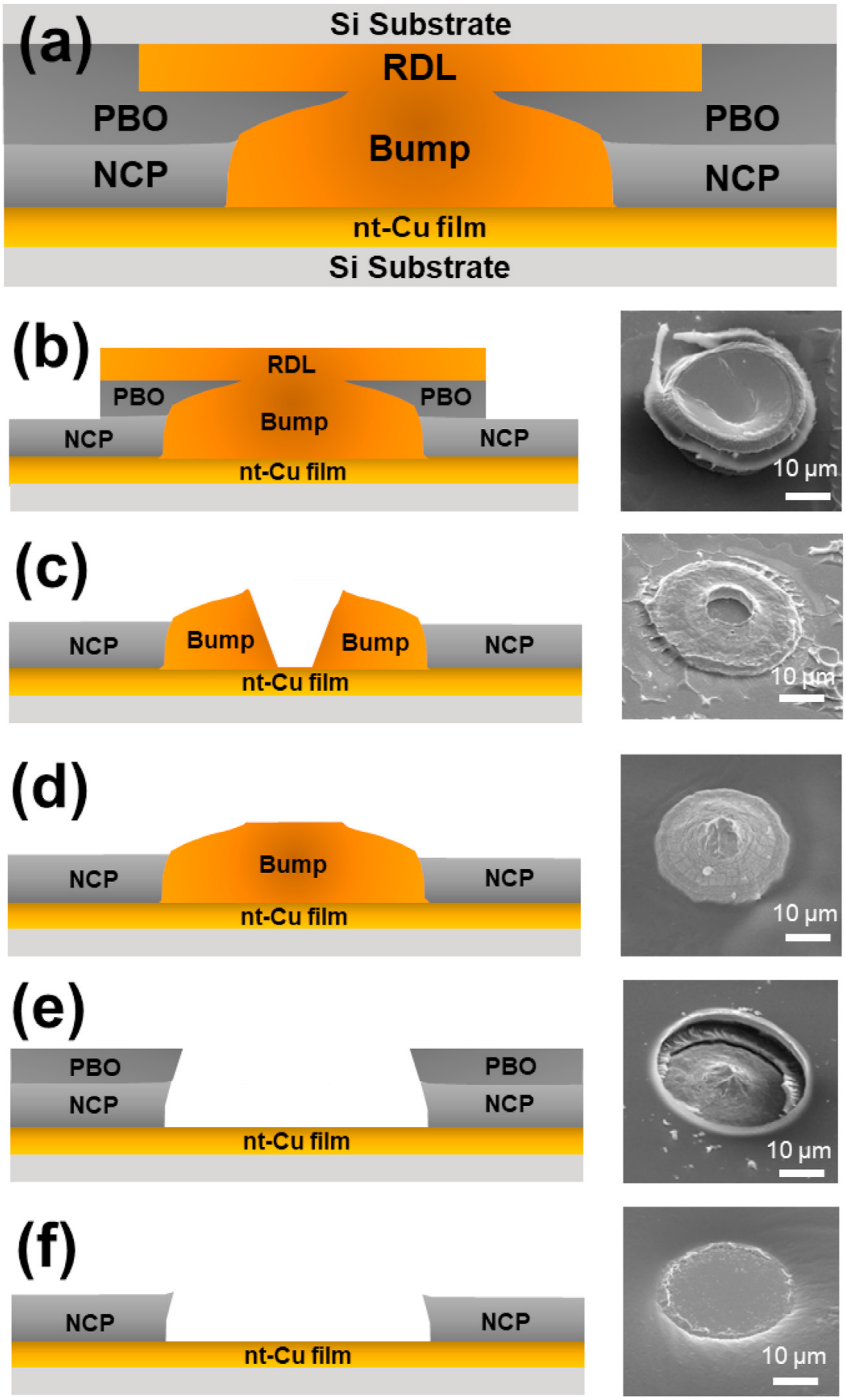

Fig. 12 – Schematic diagrams and SEM images of the fracture modes of the microbumps. (a) An ideal bonding between the bump and nt-Cu film. (b,c,d,e,f) are RDL, volcano-shaped, passivation opening, polymer layer peeling, and bonding interface fractures, respectively.

Obviously, the fracture modes of the Cu–Cu microbumps and the bonded samples are different, as shown in Figs. 11 and 12. In this study, we aimed to investigate the fracture modes with and without NCP using a bump-to-film structure and to correlate these with their bonding strengths. We found that various fracture modes of the Cu–Cu microbumps and bonding samples occurred in a single tested specimen. These could be ascribed to the non-uniformity of bonding pressure.

4. Summary and conclusions

In summary, nt-Cu and NCP were used to fabricate the hybrid Cu-to-Cu microbumps without underfilling. We employed various thermal strategies to tailor and correlate them with their microstructures and bonding properties. It was found that the heating rate influenced the void formation in the

cured NCP as a result of the rapid outgassing of solvent. By tuning the heating rate, the filling process of the NCP could be optimized. A post-annealing treatment was employed to fully cure the NCP and microbumps. Under such a thermal treatment, recrystallization and grain growth occurred and strengthened the hybrid Cu-to-Cu joints. The results show that their bonding interfaces were partially eliminated after a post-annealing treatment. Additionally, the fracture modes of the bonded samples were characterized and correlated with their bonding strengths. Taking advantage of the nt-Cu and NCP, such low budget hybrid bonding could be achieved in a non-vacuum environment at a low temperature. Thus, they can be widely applied to the mass production of the advanced ultra-fine pitch devices.

Data availability

The raw/processed data required to reproduce these findings cannot be shared at this time due to legal or ethical reasons.

Declaration of Competing Interest

The authors declare no conflict of interest.

Acknowledgements

This research was financially supported by the Ministry of Science and Technology, Taiwan under contracts, MOST 110-2221-E-A49-075-MY3 and MOST 110-2634-F-009-027; "Center for Semiconductor Technology Research" from The Featured Areas Research Center Program within the framework of the Higher Education Sprout Project by the Ministry of Education (MOE) in Taiwan; and Semiconductor Research Corporation (SRC), USA.

REFERENCES

[1] Ramm P, Bollmann D, Braun R, Buchner R, Cao-Minh U, Engelhardt M, et al. Three dimensional metallization for vertically integrated circuits: invited lecture. Microelectron Eng 1997;37:39. https://doi.org/10.1016/S0167-9317(97)00092-0.

[2] Kurino H, Lee K, Nakamura T, Sakuma K, Park K, Miyakawa N, et al. Intelligent image sensor chip with three dimensional structure. Int Electron Devices Meeting 1999. Technical Digest (Cat. No. 99CH36318) 1999:879. https://doi.org/10.1109/IEDM.1999.824289.

[3] Tu K-N, Liu Y. Recent advances on kinetic analysis of solder joint reactions in 3D IC packaging technology. Mater Sci Eng R Rep 2019;136:1–12. https://doi.org/10.1016/j.mser.2018.09.002.

[4] Chen C, Yu D, Chen K-N. Vertical interconnects of microbumps in 3D integration. MRS Bull 2015;40(3):257–63. https://doi.org/10.1557/mrs.2015.29.

[5] Iyer SS. Three-dimensional integration: an industry perspective. MRS Bull 2015;40(3):225–32. https://doi.org/10.1557/mrs.2015.32.

[6] Huang Z, Hao Y, Li Y, Hu H, Wang C, Nomoto A, et al. Three-dimensional integrated stretchable electronics. Nat Electron 2018;1(8):473–80. https://doi.org/10.1038/s41928-018-0116-y.

[7] Shen W-W, Chen K-N. Three-dimensional integrated circuit (3D IC) key technology: through-silicon via (TSV). Nanoscale Res Lett 2017;12(1):1–9. https://doi.org/10.1186/s11671-017-1831-4.

[8] Gu S. Material innovation opportunities for 3D integrated circuits from a wireless application point of view. MRS Bull 2015;40(3):233–41. https://doi.org/10.1557/mrs.2015.9.

[9] Benkart P, Kaiser A, Munding A, Bschorr M, Pfleiderer H-J, Kohn E, et al. 3D chip stack technology using through-chip interconnects. IEEE Des Test Computers 2005;22(6):512–8. https://doi.org/10.1109/MDT.2005.125.

[10] Davis WR, Wilson J, Mick S, Xu J, Hua H, Mineo C, et al. Demystifying 3D ICs: the pros and cons of going vertical. IEEE Des Test Computers 2005;22(6):498–510. https://doi.org/10.1109/MDT.2005.136.

[11] Liang Y, Chen C, Tu K-N. Side wall wetting induced void formation due to small solder volume in microbumps of Ni/SnAg/Ni upon reflow. ECS Solid State Lett 2012;1(4):P60. https://doi.org/10.1149/2.002204ssl.

[12] Lin J-A, Lin C-K, Liu C-M, Huang Y-S, Chen C, Chu D-T, et al. Formation mechanism of porous Cu_3Sn intermetallic compounds by high current stressing at high temperatures in low-bump-height solder joints. Crystals 2016;6(1):12. https://doi.org/10.3390/cryst6010012.

[13] Mo C-C, Tran D-P, Juang J-Y, Chen C. Effect of intermetallic compound bridging on the cracking resistance of $Sn_{2.3}Ag$ microbumps with different ubm structures under thermal cycling. Metals 2021;11(7):1065. https://doi.org/10.3390/met11071065.

[14] Chang Y, Chiang T, Chen C. Effect of void propagation on bump resistance due to electromigration in flip-chip solder joints using Kelvin structure. Appl Phys Lett 2007;91(13):132113. https://doi.org/10.1063/1.2790376.

[15] Chiu W-L, Liu C-M, Haung Y-S, Chen C. Formation of nearly void-free Cu3Sn intermetallic joints using nanotwinned Cu metallization. Appl Phys Lett 2014;104(17):171902. https://doi.org/10.1063/1.4874608.

[16] Lin H-W, Lu C-L, Liu C-M, Chen C, Chen D, Kuo J-C, et al. Microstructure control of unidirectional growth of η-Cu_6Sn_5 in microbumps on <111>-oriented and nanotwinned Cu. Acta Mater 2013;61(13):4910–9. https://doi.org/10.1016/j.actamat.2013.04.056.

[17] Kim T, Howlader M, Itoh T, Suga T. Room temperature Cu–Cu direct bonding using surface activated bonding method. J Vac Sci Technol 2003;21(2):449–53. https://doi.org/10.1116/1.1537716.

[18] Tan C-S, Lim D-F, Singh S-G, Goulet S, Bergkvist M. Cu–Cu diffusion bonding enhancement at low temperature by surface passivation using self-assembled monolayer of alkane-thiol. Appl Phys Lett 2009;95(19):92108. https://doi.org/10.1063/1.3263154.

[19] Huang Y-P, Chien Y-S, Tzeng R-N, Chen K-N. Demonstration and electrical performance of Cu–Cu bonding at 150 °C with Pd passivation. IEEE Trans Electron Dev 2015;62(8):2587–92. https://doi.org/10.1109/TED.2015.2446507.

[20] Liu D, Chen P-C, Liu Y-W, Hu H-W, Chen K-N. Low-temperature (70 °C) Cu-to-Cu direct bonding by capping metal layers. IEEE Electron Device Lett 2021;42(10):1524–7. https://doi.org/10.1109/LED.2021.3105434.

[21] Tsai Y-C, Hu H-W, Chen K-N. Low temperature copper-copper bonding of non-planarized copper pillar with passivation. IEEE Electron Device Lett 2020;41(8):1229–32. https://doi.org/10.1109/LED.2020.3001163.

[22] Shie K-C, Gusak AM, Tu K-N, Chen C. A kinetic model of copper-to-copper direct bonding under thermal

compression. J Mater Res Technol 2021;15:2332–44. https://doi.org/10.1016/j.jmrt.2021.09.071.
[23] Juang J-Y, Lu C-L, Chen K-J, Chen CC-A, Hsu P-N, Chen C, et al. Copper-to-copper direct bonding on highly (111)-oriented nanotwinned copper in no-vacuum ambient. Sci Rep 2018;8(1):1–11. https://doi.org/10.1038/s41598-018-32280-x.
[24] Rebhan B, Hingerl K. Physical mechanisms of copper-copper wafer bonding. J Appl Phys 2015;118(13):135301. https://doi.org/10.1063/1.4932146.
[25] Noma H, Kamibayashi T, Kuwae H, Suzuki N, Nonaka T, Shoji S, et al. Compensation of surface roughness using an Au intermediate layer in a Cu direct bonding process. J Electron Mater 2018;47(9):5403–9. https://doi.org/10.1007/s11664-018-6428-x.
[26] Ong J-J, Tran D-P, Yang S-C, Shie K-C, Chen C. Shearing characteristics of Cu-Cu joints fabricated by two-step process using highly< 111>-oriented nanotwinned Cu. Metals 2021;11(11):1864. https://doi.org/10.3390/met11111864.
[27] Shie K-C, Hsu P-N, Li Y-J, Tran D-P, Chen C. Failure mechanisms of Cu–Cu bumps under thermal cycling. Materials 2021;14(19):5522. https://doi.org/10.3390/ma14195522.
[28] Han H, Lee C, Kim Y, Lee J, Kim R, Kim J, et al. Cu to Cu direct bonding at low temperature with high density defect in electrodeposited Cu. Appl Surf Sci 2021;550:149337. https://doi.org/10.1016/j.apsusc.2021.149337.
[29] Chang L-P, Wang J-J, Hung T-H, Chen K-N, Ouyang F-Y. Direct metal bonding using nanotwinned Ag films with (111) surface orientation under air atmosphere for heterogeneous integration. Appl Surf Sci 2021;576:151845. https://doi.org/10.1016/j.apsusc.2021.151845.
[30] Zhang L, Liu Z-Q, Chen S-W, Wang Y-D, Long W-M, Guo Y-H, et al. Materials, processing and reliability of low temperature bonding in 3D chip stacking. J Alloys Compd 2018;750:980–95. https://doi.org/10.1016/j.jallcom.2018.04.040.
[31] Kagawa Y, Fujii N, Aoyagi K, Kobayashi Y, Nishi S, Todaka N, et al. Novel stacked CMOS image sensor with advanced Cu2Cu hybrid bonding. 2016 IEEE Int Electron Devices Meeting (IEDM) 2016:8.4. 1–8.4. 4. https://doi.org/10.1109/IEDM.2016.7838375. IEEE.
[32] Ko C-T, Chen K-N. Low temperature bonding technology for 3D integration. Microelectron Reliab 2012;52(2):302–11. https://doi.org/10.1016/j.microrel.2011.03.038.
[33] Ko C-T, Chen K-N. Reliability of key technologies in 3D integration. Microelectron Reliab 2013;53(1):7–16. https://doi.org/10.1016/j.microrel.2012.08.011.
[34] Hsiao H-Y, Liu C-M, Lin H-W, Liu T-C, Lu C-L, Huang Y-S, et al. Unidirectional growth of microbumps on (111)-oriented and nanotwinned copper. Science 2012;336(6084):1007–10. https://doi.org/10.1126/science.1216511.
[35] Tran D-P, Chen K-J, Tu K-N, Chen C, Chen Y-T, Chung S. Electrodeposition of slanted nanotwinned Cu foils with high strength and ductility. Electrochim Acta 2021;389:138640. https://doi.org/10.1016/j.electacta.2021.138640.
[36] Cheng H-Y, Tran D-P, Tu K-N, Chen C. Effect of deposition temperature on mechanical properties of nanotwinned Cu fabricated by rotary electroplating. Mater Sci Eng, A 2021;811:141065. https://doi.org/10.1016/j.msea.2021.141065.
[37] Hung Y-W, Tran D-P, Chen C. Effect of Cu ion concentration on microstructures and mechanical properties of nanotwinned Cu foils fabricated by rotary electroplating. Nanomaterials 2021;11(8):2135. https://doi.org/10.3390/nano11082135.
[38] Lu L, Shen Y, Chen X, Qian L, Lu K. Ultrahigh strength and high electrical conductivity in copper. Science 2004;304(5669):422–6. https://doi.org/10.1126/science.1092905.
[39] Tseng I-H, Hsu Y-T, Leu J, Tu K-N, Chen C. Effect of thermal stress on anisotropic grain growth in nano-twinned and un-twinned copper films. Acta Mater 2021;206:116637. https://doi.org/10.1016/j.actamat.2021.116637.
[40] Tseng C-H, Tseng I-H, Huang Y-P, Hsu Y-T, Leu J, Tu K-N, et al. Kinetic study of grain growth in highly (111)-preferred nanotwinned copper films. Mater Char 2020;168:110545. https://doi.org/10.1016/j.matchar.2020.110545.
[41] Tseng I-H, Hsu P-N, Hsu W-Y, Tran D-P, Lin BT-H, Chang C-C, et al. Effect of oxidation on electromigration in 2-μm Cu redistribution lines capped with polyimide. Results Phys 2021;31:105048. https://doi.org/10.1016/j.rinp.2021.105048.
[42] Tseng I-H, Hsu P-N, Lu T-L, Tu K-N, Chen C. Electromigration failure mechanisms of <111>-oriented nanotwinned Cu redistribution lines with polyimide capping. Results Phys 2021;24:104154. https://doi.org/10.1016/j.rinp.2021.104154.
[43] Tran D-P, Li H-H, Tseng I-H, Chen C. Enhancement of electromigration lifetime of copper lines by eliminating nanoscale grains in highly <111>-oriented nanotwinned structures. J Mater Res Technol 2021;15:6690–9. https://doi.org/10.1016/j.jmrt.2021.11.111.
[44] Shen F-C, Huang C-Y, Lo H-Y, Hsu W-Y, Wang C-H, Chen C, et al. Atomic-scale investigation of electromigration with different directions of electron flow into high-density nanotwinned copper through in situ HRTEM. Acta Mater 2021;219:117250. https://doi.org/10.1016/j.actamat.2021.117250.
[45] Liu C-M, Lin H-W, Huang Y-S, Chu Y-C, Chen C, Lyu D-R, et al. Low-temperature direct copper-to-copper bonding enabled by creep on (111) surfaces of nanotwinned Cu. Sci Rep 2015;5(1):1–11. https://doi.org/10.1038/srep09734.
[46] Liu C-M, Lin H-W, Chu Y-C, Chen C, Lyu D-R, Chen K-N, et al. Low-temperature direct copper-to-copper bonding enabled by creep on highly (111)-oriented Cu surfaces. Scripta Mater 2014;78:65–8. https://doi.org/10.1016/j.scriptamat.2014.01.040.
[47] Agrawal PM, Rice BM, Thompson DL. Predicting trends in rate parameters for self-diffusion on FCC metal surfaces. Surf Sci 2002;515(1):21–35. https://doi.org/10.1016/S0039-6028(02)01916-7.
[48] Tseng C-H, Tu K-N, Chen C. Comparison of oxidation in uni-directionally and randomly oriented Cu films for low temperature Cu-to-Cu direct bonding. Sci Rep 2018;8(1):1–7. https://doi.org/10.1038/s41598-018-28812-0.
[49] Kuo Y-H, Chen C. Hybrid Cu-Cu bonding with non-conductive paste and highly (111)-oriented nanotwinned copper. 2020 15th Int Microsystems, Packaging Assembly and Circuits Technol Conf (IMPACT) 2020:259–61. https://doi.org/10.1109/IMPACT50485.2020.9268547. IEEE.
[50] Wong C, Shi S-H, Jefferson G. High performance no-flow underfills for low-cost flip-chip applications: material characterization. IEEE Trans Compon Packag Manuf Technol 1998;21(3):450–8. https://doi.org/10.1109/95.725209.
[51] Chiu W-L, Lee O-H, Chiang C-W, Chang H-H. Low temperature wafer-to-wafer hybrid bonding by nanotwinned copper. 2021 IEEE 71st Electronic Components Technol Conf (ECTC) 2021:365–70. https://doi.org/10.1109/ECTC32696.2021.00068. IEEE.
[52] Shie K-C, He P-S, Kuo Y-H, Ong J-J, Tu K-N, Lin BT-H, et al. Hybrid bonding of nanotwinned copper/organic dielectrics with low thermal budget. 2021 IEEE 71st Electronic Components Technol Conf (ECTC) 2021:432–7. https://doi.org/10.1109/ECTC32696.2021.00079. IEEE.
[53] Ehlers GFL, Fisch KR, Powell WR. The thermal breakdown mechanism of polybenzoxazoles and polybenzothiazoles. J Polym Sci: Symposium 1973;43:55–75. https://doi.org/10.1002/polc.5070430108.

[54] Alpha NCX PRL-507 product, MacDermid Alpha Electronics Solutions, https://www.macdermidalpha.com/semiconductor-solutions/products/solder-flux/alphar-ncx-prl507. Accessed on 01/2022.
[55] Liu D, Chen P-C, Chou T-C, Hu H-W, Chen K-N. Demonstration of low-temperature fine-pitch Cu/SiO_2 hybrid bonding by Au passivation. IEEE J Electron Devices Soc 2021;9:868–75. https://doi.org/10.1109/JEDS.2021.3114648.
[56] Kang Q, Wang C, Li G, Zhou S, Tian Y. Low-temperature Cu/SiO2 hybrid bonding using a novel two-step cooperative surface activation. 2021 22nd Int Conf Electronic Packaging Technol (ICEPT) 2021:1–5. https://doi.org/10.1109/ICEPT52650.2021.9568007.
[57] Ong J-J, Shie K-C, Chen C. Microstructure analysis and tensile strength of low temperature Cu bonds using highly-<111> Cu. 2021 7th Int Workshop Low Temperature Bonding for 3D Integration (LTB-3D) 2021:25. https://doi.org/10.1109/LTB-3D53950.2021.9598367.
[58] Hung T-H, Kang T-C, Mao S-Y, Chou T-C, Hu H-W, Chiu H-Y, et al. Investigation of wet pretreatment to improve Cu-Cu bonding for hybrid bonding applications. 2021 IEEE 71st Electronic Components Technol Conf (ECTC) 2021:700–5. https://doi.org/10.1109/ECTC32696.2021.00121.
[59] He R, Fujino M, Yamauchi A, Suga T. Combined surface-activated bonding technique for low-temperature hydrophilic direct wafer bonding. Jpn J Appl Phys 2016;55(4S):04EC02. https://doi.org/10.7567/JJAP.55.04EC02.